Scattering blanketing effect of Earth's proto-atmosphere: enhanced suppression of planetary radiation and magma ocean cooling

Tatsuya Yoshida,[1] Kirara Arima,[2] Takeshi Kuroda,[1,3] Naoki Terada,[1] and Kiyoshi Kuramoto[2]

[1]*Faculty of Science, Tohoku University, Sendai, Miyagi 980-8578, Japan*
[2]*Faculty of Science, Hokkaido University, Sapporo, Hokkaido 060-0810, Japan*
[3]*Division for the Establishment of Frontier Sciences of Organization for Advanced Studies, Tohoku University, Sendai, Miyagi 980-8577, Japan*

ABSTRACT

The thermal evolution of magma oceans formed by giant impacts is strongly influenced by a proto-atmosphere through its blanketing effect, which suppresses outgoing planetary radiation. While both radiative absorption and Rayleigh scattering by atmospheric species can contribute to this effect, the role of the scattering in suppressing thermal radiation from magma oceans remains unclear. In this study, we developed a 1-D radiative transfer model for planetary and solar radiation in a proto-atmosphere composed of H_2O and H_2, and a coupled thermal evolution model of a planetary interior and proto-atmosphere, to investigate the scattering blanketing effect on planetary radiation and magma ocean cooling. Our results show that Rayleigh scattering significantly reduces outgoing planetary radiation at wavelengths below $\sim 1\,\mu$m, particularly in hot, thick atmospheres where scattering is highly effective. Consequently, the planetary outgoing radiation flux decreases by up to about one to two orders of magnitude, and the magma ocean lifetime is prolonged by up to about three times due to the scattering blanketing effect when the total amounts of H_2O and H_2 are equivalent to or greater than the present-day terrestrial seawater. These findings suggest that the prolonged magma ocean phase facilitated efficient differentiation between compatible and incompatible elements, even in the lower mantle. Furthermore, they imply that sustained magma oceans likely persisted throughout much of the giant impact phase, supporting a magma ocean origin of the Moon consistent with its observed chemical characteristics.

Keywords: Planetary science (1255) — Planetary atmospheres (1244) — Atmospheric evolution (2301)

1. INTRODUCTION

Planet formation theories suggest that Earth-sized planets likely underwent a globally molten state due to giant impacts during the late stages of accretion (e.g., Canup 2004a; Zahnle et al. 2007; Solomatov 2007; Elkins-Tanton 2012). This magma ocean would have cooled primarily through thermal radiation into space. The cooling process is known to be strongly influenced by the properties of proto-atmospheres, particularly through their blanketing effects. The role of steam atmospheres in this context has been extensively studied (Abe & Matsui 1985, 1986, 1988; Matsui & Abe 1986a,b; Zahnle et al. 1988; Elkins-Tanton 2008, 2012; Lebrun et al. 2013; Hamano et al. 2013, 2015; Massol et al. 2016, 2023; Schaefer et al. 2016; Salvador et al. 2017; Marcq et al. 2017; Ikoma et al. 2018; Bower et al. 2019; Katyal et al. 2019; Nikolaou et al. 2019; Pluriel et al. 2019; Barth et al. 2021; Lichtenberg et al. 2021). These atmospheres can drastically lower the outgoing planetary radiation flux by several orders of magnitude compared to blackbody radiation, due to the infrared-absorbing properties of H_2O (e.g., Kasting 1988; Nakajima et al. 1992; Goldblatt et al. 2013). Consequently, the presence of thick steam atmospheres with masses comparable to or exceeding Earth's current ocean mass can extend the lifetime of the magma ocean to several million years at Earth's orbital distance (e.g., Lebrun et al. 2013; Hamano et al. 2013).

Recent studies have examined magma ocean evolution across a wide range of atmospheric compositions by considering diverse oxygen fugacities in magma ocean-atmosphere systems (Katyal et al. 2020; Lichtenberg et al. 2021; Bower et al. 2022; Maurice et al. 2024; Nicholls et al. 2024, 2025). Lichtenberg et al. (2021) investigated the blanketing effects of individual atmospheric species of H_2O, H_2, CO_2, CH_4, CO, O_2, and N_2 by modeling single-component atmospheres. Their findings indicate that H_2 exhibits particularly strong blanketing effects due to collision-induced absorption at high-pressure conditions: the solidification of the magma ocean beneath an H_2 atmosphere with a mass of the present-day terrestrial seawater is not completed within 100 million years even at the Earth's orbit.

In addition to radiative absorption, scattering of planetary radiation can also contribute to the blanketing effect. Rayleigh scattering becomes significant at shorter wavelengths; for instance, the Rayleigh scattering cross-section of H_2O exceeds its absorption cross-section at wavelengths below $\sim 0.5\,\mu m$ (e.g., Pierrehumbert 2010; Rothman et al. 2013). As suggested by the blackbody spectrum, the contribution of thermal radiation at such short wavelengths, influenced by Rayleigh scattering, increases with the surface temperature. Consequently, Rayleigh scattering by atmospheric species is expected to reduce outgoing planetary radiation from a hot magma ocean, potentially extending the magma ocean's lifetime. Although some previous studies on the thermal evolution with steam atmospheres considered the Rayleigh scattering of planetary radiation (e.g., Abe & Matsui 1988; Zahnle et al. 1988; Goldblatt et al. 2013; Hamano et al. 2015), the specific impact on thermal radiation from magma oceans remains unclear.

In this study, we developed a 1-D radiative transfer model for planetary and solar radiation in a proto-atmosphere composed of H_2O and H_2, incorporating both radiative absorption and scattering processes, to investigate the scattering blanketing effect on thermal planetary radiation. Additionally, to estimate the thermal evolution of a magma ocean and proto-atmosphere, we coupled the radiative transfer model with a planetary interior model that accounts for thermal structure and volatile partitioning. The remainder of this paper is organized as follows: in Section 2, we describe our 1-D radiative transfer model and the coupled thermal evolution model of the magma ocean and atmosphere. Section 3.1 presents the numerical results for planetary and solar radiation transfer in proto-atmospheres composed of H_2O and H_2, with a focus on the scattering blanketing effect. Section 3.2 shows the thermal co-evolution of an H_2O-H_2 proto-atmosphere and magma ocean. Section 4.1 examines the effects of uncertainties in atmospheric structure assumptions. Section 4.2 discusses the chemical evolution of proto-atmosphere and magma ocean. Section 4.3 describes the effects of our results on chemical differentiation in a magma ocean. Section 4.4 discusses the implications of our results for the Moon's origin.

2. MODEL DESCRIPTION

2.1. *Atmospheric structure*

We suppose that atmospheres are composed of H_2O and H_2, which are expected to be major radiative absorption sources in proto-atmospheres (Lichtenberg et al. 2021). The atmosphere in hydrostatic equilibrium is vertically divided into 500 layers from the ground to the top of the atmosphere, which are equally spaced on a logarithmic scale of pressure. The pressure at the top of the atmosphere is fixed at 1 Pa. We treat H_2 as an ideal gas and H_2O as a non-ideal gas following the Peng-Robinson equation of state (Peng & Robinson 1976), in a similar manner to Abe & Matsui (1988) and Hamano et al. (2015). The Peng-Robinson equation of state is described as follows:

$$P = \frac{RT}{V - b} - \frac{a(T)}{V(V + b) + b(V - b)},\tag{1}$$

where P is the pressure, R is the gas constant, T is the temperature, and V is the molar volume (Peng & Robinson 1976). Here $a(T)$ and b are defined by

$$a(T) = 0.45724\frac{R^2T_c^2}{P_c}\left[1 + \kappa\left(1 - \sqrt{\frac{T}{T_c}}\right)\right]^2,\tag{2}$$

$$b = 0.07780\frac{RT_c}{P_c},\tag{3}$$

$$\kappa = 0.37464 + 1.54226\omega_a - 0.26992\omega_a^2,\tag{4}$$

where T_c and P_c are the temperature and pressure at the critical point, respectively, and ω_a is the acentric factor. Here $P_c = 2.204 \times 10^7\,Pa$, $T_c = 647.3\,K$, and $\omega_a = 0.344$ for H_2O (e.g., Chase 1998).

The surface temperature is varied from 200 K to 4000 K during the course of the radiative transfer calculations. The temperature profile in the lower part of the atmosphere is supposed to follow an adiabatic lapse rate, and that in the upper part is given by the skin temperature, which is the asymptotic temperature at high altitudes of an upper atmosphere that is optically thin in the thermal-IR and transparent to shortwave radiation. The lapse rate is assumed to be a dry adiabat for atmospheric layers in which the temperature is above the critical temperature of H_2O or the relative humidity is less than 1. The dry adiabatic lapse rate is given by

$$\left(\frac{\partial T}{\partial P}\right)_{\text{dry}} = \frac{\rho_v T}{\rho_v C_{p,v} + \rho_n C_{p,n}}\left(\frac{\partial(1/\rho_v)}{\partial T}\right)_P,\tag{5}$$

where ρ_v and ρ_n are the densities of the condensible gas and non-condensible gas, respectively, $C_{p,v}$ and $C_{p,n}$ are the constant-pressure specific heat of the condensible gas and non-condensible gas, respectively (Kasting 1988; Marcq 2012; Marcq et al.

2017). For the layers where the relative humidity is unity, the lapse rate is given by a pseudo-moist adiabat as given by

$$\left(\frac{\partial T}{\partial P}\right)_{\text{moist}} = \left[\frac{dP_s}{dT} + \frac{\rho_n R}{M_n}\left(1 + \frac{d\ln\rho_v}{d\ln T} - \frac{d\ln(\rho_v/\rho_n)}{d\ln T}\right)\right]^{-1}, \tag{6}$$

where P_s is the saturation vapor pressure of H_2O and M_n is the molecular weight of the non-condensible gas (Kasting 1988; Marcq 2012; Wordsworth & Pierrehumbert 2013; Marcq et al. 2017). Here,

$$\frac{d\ln(\rho_v/\rho_n)}{d\ln T} = \frac{1}{(\rho_v/\rho_n)(s_v - s_c) + R/M_n}\left[\frac{R}{M_n}\frac{d\ln\rho_v}{d\ln T} - C_{v,n} - \frac{\rho_v}{\rho_n}\left(\frac{ds_v}{d\ln T}\right)\right], \tag{7}$$

where s_v and s_c are the specific entropies of the vapor phase and the condensed phase, respectively (Kasting 1988). When the temperature reaches the skin temperature, the temperature above is assumed to be constant at the skin temperature as given by

$$T_{\text{skin}} = \left(\frac{F_{\text{OLR}}}{2\sigma}\right)^{1/4}, \tag{8}$$

where σ is the Stefan-Boltzmann constant and F_{OLR} is the outgoing longwave radiation flux. The method to obtain F_{OLR} is described in the next subsection. We conducted iterative procedures to calculate T_{skin} and F_{OLR} self-consistently.

We refer to the temperature-dependent specific heat, entropy, and latent heat data provided in the NIST Chemistry WebBook (Chase 1998). The saturation vapor pressure of H_2O is given by Osborne-Mayers and Washburn formula in the same manner as Abe & Matsui (1988). At $273.15\,\text{K} \leq T \leq 647.26\,\text{K}$,

$$\ln P_s(T) = \alpha - \frac{\beta}{t} + \frac{\gamma x}{t}[\exp(\delta x^2) - 1] - \epsilon\exp(-\eta y), \tag{9}$$

where $t = T + 0.01$, $x = t^2 - 293700$, $y = (647.26 - T)^{5/4}$, $\alpha = 24.021415$, $\beta = 4616.9134$, $\gamma = 3.1934553 \times 10^{-4}$, $\delta = 2.7550431 \times 10^{-11}$, $\epsilon = 1.0246503 \times 10^{-2}$, and $\eta = 1.3158813 \times 10^{-2}$ (Eisenberg & Kauzmann 1969; Abe & Matsui 1988). At $T \leq 273.15\,\text{K}$,

$$\ln P_s(T) = \alpha' - \frac{\beta'}{t} + \gamma'\log t - \delta't + \epsilon't^2, \tag{10}$$

where $t = T - 0.05$, $\alpha' = -10.666189$, $\beta' = 5631.1206$, $\gamma' = 18.953038$, $\delta' = 3.8614490 \times 10^{-2}$, and $\epsilon' = 2.7749374 \times 10^{-5}$ (Abe & Matsui 1988).

2.2. Radiative transfer calculations

We solve the radiative transfer equation in a plane-parallel atmosphere on the two-stream approximation (Toon et al. 1989) for the planetary and stellar radiation separately:

$$\frac{\partial F_\nu^+}{\partial \tau_\nu} = \gamma_1 F_\nu^+ - \gamma_2 F_\nu^- - S_\nu^+, \tag{11}$$

$$\frac{\partial F_\nu^-}{\partial \tau_\nu} = \gamma_2 F_\nu^+ - \gamma_1 F_\nu^- + S_\nu^-, \tag{12}$$

where ν is the wavenumber, τ_ν is the optical depth at ν, F_ν^+ and F_ν^- are the upward and downward radiative fluxes at ν, and γ_i is the coefficient which depends upon the particular form of the two-stream equation, respectively. For the planetary radiation,

$$S_\nu^+ = S_\nu^- = 2\pi(1 - \omega_0)B_\nu(T), \tag{13}$$

where ω_0 is the single scattering albedo and $B_\nu(T)$ is the Planck function. For the solar flux,

$$S_\nu^+ = \gamma_3 F_\nu^s \omega_0 \exp\left(-\frac{\tau_\nu}{\mu_0}\right), \tag{14}$$

$$S_\nu^- = (1 - \gamma_3)F_\nu^s \omega_0 \exp\left(-\frac{\tau_\nu}{\mu_0}\right), \tag{15}$$

where F_ν^s is the incoming solar flux at ν, τ_ν is the optical depth from the top of the atmosphere at ν, and μ_0 is the cosine of the mean stellar zenith angle ($57.3°$) (e.g., Hu et al. 2012). Following the recommendation by Toon et al. (1989), we use the

hemispheric mean method for planetary radiation and the quadrature method for solar radiation. Here $\gamma_1 = 2 - \omega_0$ and $\gamma_2 = \omega_0$ in the hemispheric mean method, and $\gamma_1 = \sqrt{3}(2 - \omega_0)/2$, $\gamma_2 = \sqrt{3}\omega_0/2$, and $\gamma_3 = 1/2$ in the quadrature method (Toon et al. 1989).

As radiative absorption sources, we consider line and continuum absorption of H_2O and collision-induced absorption of H_2-H_2. We use the H_2O line data in HITEMP 2010 (Rothman et al. 2010). The line profile of H_2O is assumed to follow a Voigt profile, truncated at 25 cm^{-1} from the line center, to combine with continuum absorption represented by the MT_CKD 4.2 model (Mlawer et al. 2023) without double-counting. Here we use EXOCROSS (Yurchenko et al. 2018) for the line profile calculations. We use the H_2-H_2 collision-induced absorption data provided by Borysow et al. (2001) and Borysow (2002). We also consider Rayleigh scattering by H_2O and H_2. The scattering cross-section is given by

$$\sigma_i^s(\lambda) = \frac{128\pi^5(\alpha_i^p)^2}{3\lambda^4}, \tag{16}$$

where λ is the wavelength, and σ_i^s and α_i^p are the scattering cross-section and the polarizability constant of species i, respectively (e.g., Pierrehumbert 2010). Here $\alpha_{H_2O}^p = 1.50$ Å^3 and $\alpha_{H_2}^P = 0.787$ Å^3, respectively (Johnson 1998). Considering the absorption and scattering by the atmosphere, the optical depth τ_ν is calculated by

$$\frac{d\tau_\nu}{dP} = \frac{1}{\rho g}\left[\sum_i(\sigma_i^a(\nu) + \sigma_i^s(\nu))n_i + k_{H_2-H_2}(\nu)n_{H_2}^2\right], \tag{17}$$

where ρ is the atmospheric mass density, g is the gravitational acceleration, n_i is the number density of species i, $\sigma_i^a(\nu)$ and $\sigma_i^s(\nu)$ are the absorption and scattering cross-sections at ν of species i, and $k_{H_2-H_2}(\nu)$ is the absorption coefficient of the H_2-H_2 collision-induced absorption at ν, respectively.

By calculating the scattered upward flux at the top of the atmosphere, we estimate the planetary albedo defined as follows:

$$A_p = \frac{F_{s,\text{top}}^+}{\mu_0 S_\odot}, \tag{18}$$

where A_p is the planetary albedo, $F_{s,\text{top}}^+$ is the scattered upward flux at the top of the atmosphere, and $S_\odot$ is the solar constant. Here we adopt the solar constant 0.7 times the present-day value considering the faint young Sun (Gough 1981). The surface albedo is assumed to be 0.2 (e.g., Kasting 1988). Note that the radiative effects of clouds are not included in this model, which may cause the estimated planetary albedo to deviate from the true 3-D average planetary albedo (see Section 4.1.3). The net absorbed solar flux is given by

$$F_{\text{Sun}} = \frac{1}{4}(1 - A_p)S_\odot. \tag{19}$$

We evaluate the integral of the radiative flux over a wavenumber range from 1 cm^{-1} to 30000 cm^{-1} with a resolution of 1 cm^{-1} by applying a line-by-line method following Schaefer et al. (2016) and Wordsworth et al. (2017). We tabulate the absorption cross-section on temperature and pressure grids. Here the temperature grids are [100, 150, 200, 250, 300, 350, 400, 450, 600, 800, 1000, 1250, 1500, 1750, 2000, 2250, 2500, 2750, 3000, 3250, 3500, 3750, 4000] K, and the pressure grids are [10^{-5}, 10^{-4}, 5×10^{-4}, 10^{-3}, 5×10^{-3}, 10^{-2}, 5×10^{-2}, 10^{-1}, 5×10^{-1}, 1, 5, 10, 50, 10^2, 5×10^2, 10^3, 5×10^3] bar.

2.3. Interior structure and energy conservation

In Section 3.2, we estimate the coupled thermal evolution of the atmosphere and the interior by combining the radiative flux depending on the surface temperature and atmospheric amount and composition. We consider a spherically symmetric hydrostatic mantle where the lower boundary is the core-mantle boundary with a depth of 2900 km and the upper boundary is the planetary surface. The mantle is initially assumed to be fully molten with a potential temperature of 4000 K. The magma ocean is convecting vigorously, so the temperature distribution is supposed to be adiabatic following Lebrun et al. (2013). As it cools, the adiabatic temperature profile intersects with the liquidus and solidus temperature profiles from the bottom. We use the solidus and liquidus curves of KLB-1 peridotite obtained from experimental data (Hirschmann 2000; Herzberg et al. 2000; Fiquet et al. 2010; Zhang & Herzberg 1994), whose fitting formula is derived by Nikolaou et al. (2019). The melt fraction at any depth is given by

$$\phi = \frac{T - T_{\text{sol}}}{T_{\text{liq}} - T_{\text{sol}}}, \tag{20}$$

where ϕ is the melt fraction, T is the temperature of the mantle at a given depth, T_{sol} is the solidus temperature, and T_{liq} is the liquidus temperature, respectively (e.g., Abe 1997; Solomatov 2007; Lebrun et al. 2013; Nikolaou et al. 2019). The adiabatic

temperature gradient is given by

$$
\left(\frac{\partial T}{\partial P}\right)_s = \begin{cases} \frac{\alpha_T T}{\rho_m C_{p,M}}, & \text{for } \phi = 1 \\ \frac{\alpha_T T}{\rho_s C_{p,M}}, & \text{for } \phi = 0 \\ \frac{\alpha_T T/\rho_M - \Delta H (\partial\phi/\partial P)_T}{C_{p,M} - \Delta H (\partial\phi/\partial T)_P}, & \text{for } 0 < \phi < 1 \end{cases} \tag{21}
$$

where ρ_m is the melt density (= 4.0×10^3 kg/m^3), ρ_s is the solid density (= 4.2×10^3 kg/m^3), ρ_M is the mean density of the melt and solid, $C_{p,M}$ is the specific heat of the mantle (= 1.0×10^3 J/kg/K), ΔH is the difference of specific enthalpy between the melt and solid phases (= 4×10^5 J/kg), and α_T is the thermal expansivity given by

$$
\alpha_T = \alpha_{T,0} \left(\frac{PK'}{K_0} + 1\right)^{-(m-1+K')/K'}, \tag{22}
$$

where $\alpha_{T,0} = 3 \times 10^{-5}$ K^{-1}, $K_0 = 200$ GPa, $K' = 4$, and $m = 0$, respectively (Abe 1997; Lebrun et al. 2013).

The coupled thermal evolution is obtained by the energy conservation equation:

$$
r^2 \rho_M \left[C_{p,M} + \Delta H \left(\frac{\partial\phi}{\partial T}\right)_P\right] \frac{\partial T}{\partial t} = \frac{\partial}{\partial r}[r^2(F_{\text{Sun}} - F_{\text{OLR}})], \tag{23}
$$

where r is the radial distance from the planetary center and F_{OLR} is the outgoing planetary radiation flux, respectively (Lebrun et al. 2013). Here the cooling from the magma ocean is supposed to be along with the net energy balance of the incoming and outgoing radiation at the top of the atmosphere (Hamano et al. 2013; Katyal et al. 2019).

2.4. *Partitioning of volatiles between the atmosphere and the interior*

In Section 3.2, the partitioning of volatiles among the solid mantle, magma ocean, and atmosphere is considered as follows:

$$
k_i X_i M_{\text{solid}} + X_i M_{\text{liquid}} + \frac{4\pi R_p^2}{g} \frac{\mu_i}{\bar{\mu}} P_i = M_i^0, \tag{24}
$$

where R_p is the planetary radius, X_i, P_i, M_i^0, μ_i, and k_i are the mass fraction in the magma ocean, atmospheric partial pressure, initial total amount, molecular weight, and distribution coefficient between the solid and liquid phases of species i, respectively, $\bar{\mu}$ is the mean molecular weight of the atmosphere, M_{solid} is the mass of the solid mantle, and M_{liquid} is the mass of the magma ocean (Lebrun et al. 2013; Bower et al. 2019; Nikolaou et al. 2019). We assume that $k_{\text{H}_2\text{O}} = k_{\text{H}_2} = 0.01$ for simplicity by referring to the values for H$_2$O used in previous studies (e.g., Lebrun et al. 2013). We use a solubility law to relate the atmospheric partial pressure and the mass fraction in the magma ocean as follows:

$$
P_i = \left(\frac{X_i}{\alpha_i}\right)^{\beta_i}, \tag{25}
$$

where α_i and β_i are the Henrian fit coefficients of species i. Here $\alpha_{\text{H}_2\text{O}} = 6.8 \times 10^{-8}$, $\beta_{\text{H}_2\text{O}} = 1.43$, $\alpha_{\text{H}_2} = 2.572 \times 10^{-6}$, and $\beta_{\text{H}_2} = 1.0$ (Lebrun et al. 2013; Lichtenberg et al. 2021).

3. RESULTS

3.1. *Radiative properties and atmospheric structure*

In this section, we illustrate the radiation properties, with a particular focus on the scattering blanketing effect. This section only considers the atmosphere with condensed seawater on the planetary surface, excluding interactions with the planetary interior described in Section 2.3 and 2.4. Outgoing longwave radiation (OLR) is presented in Figure 1, and vertical profiles of temperature, radiation flux, and optical depth are shown in Figure 2. For pure H$_2$O atmospheres, the scattering blanketing effect becomes more pronounced as surface temperature and pressure increase, as demonstrated by the differences in OLR between cases with and without scattering (Figure 1(a)). Rayleigh scattering suppresses OLR at high wavenumbers ($\gtrsim 20000$ cm^{-1}), while H$_2$O absorption dominates at lower wavenumbers (Figure 1(b)). At high temperatures, OLR increases at higher wavenumbers where Rayleigh scattering is significant (Equation (16)), enhancing the scattering blanketing effect. Additionally, high pressure is required for the scattering blanketing effect to become significant, as the optical depth at wavenumbers dominated by Rayleigh scattering reaches unity when atmospheric pressure exceeds $\sim 10^5$ Pa, as shown in the pressure at the optical depth of unity
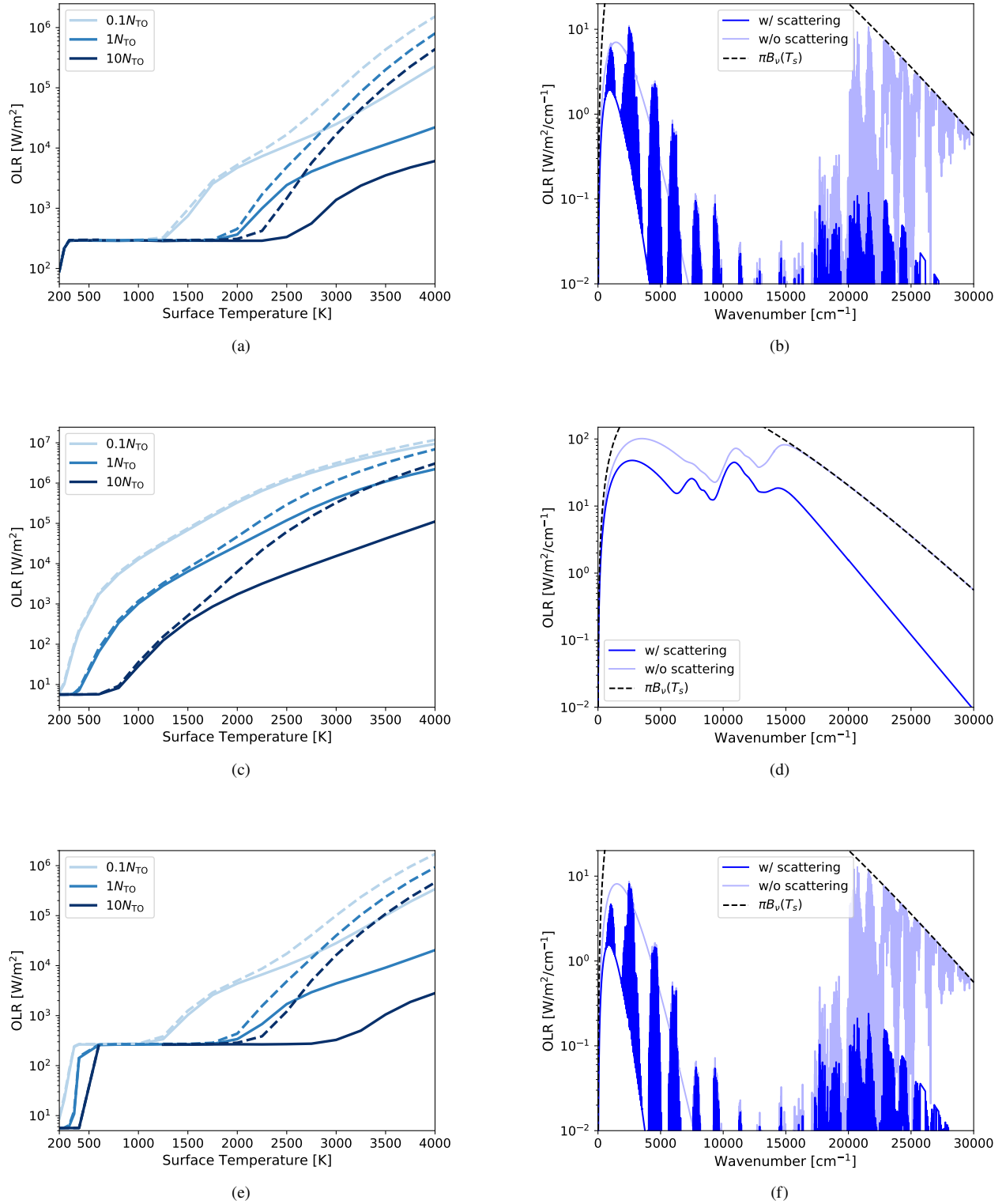
Figure 1. (a) Outgoing longwave radiation (OLR) depending on the surface temperature on pure H_2O atmospheres. The solid and dashed lines represent the OLR with and without the Rayleigh scattering blanketing effects, respectively. Line colors represent variations in the total hydrogen molecular number in the atmosphere with seawater. Here N_{TO} is the hydrogen molecular number in the present-day terrestrial seawater. (b) OLR per wavenumber when the surface temperature is 3000 K and the total hydrogen amount is N_{TO} on a pure H_2O atmosphere with seawater. The dark and light blue lines represent the OLR with and without the Rayleigh scattering blanketing effects, respectively. The dashed black line represents the blackbody spectrum with the surface temperature. (c) and (d) are the same as (a) and (b), respectively, but for the pure H_2 atmospheres. (e) and (f) are the same as (a) and (b), respectively, but for the H_2O-H_2 atmospheres with a molar H_2/H_2O ratio of unity in the atmosphere with seawater.
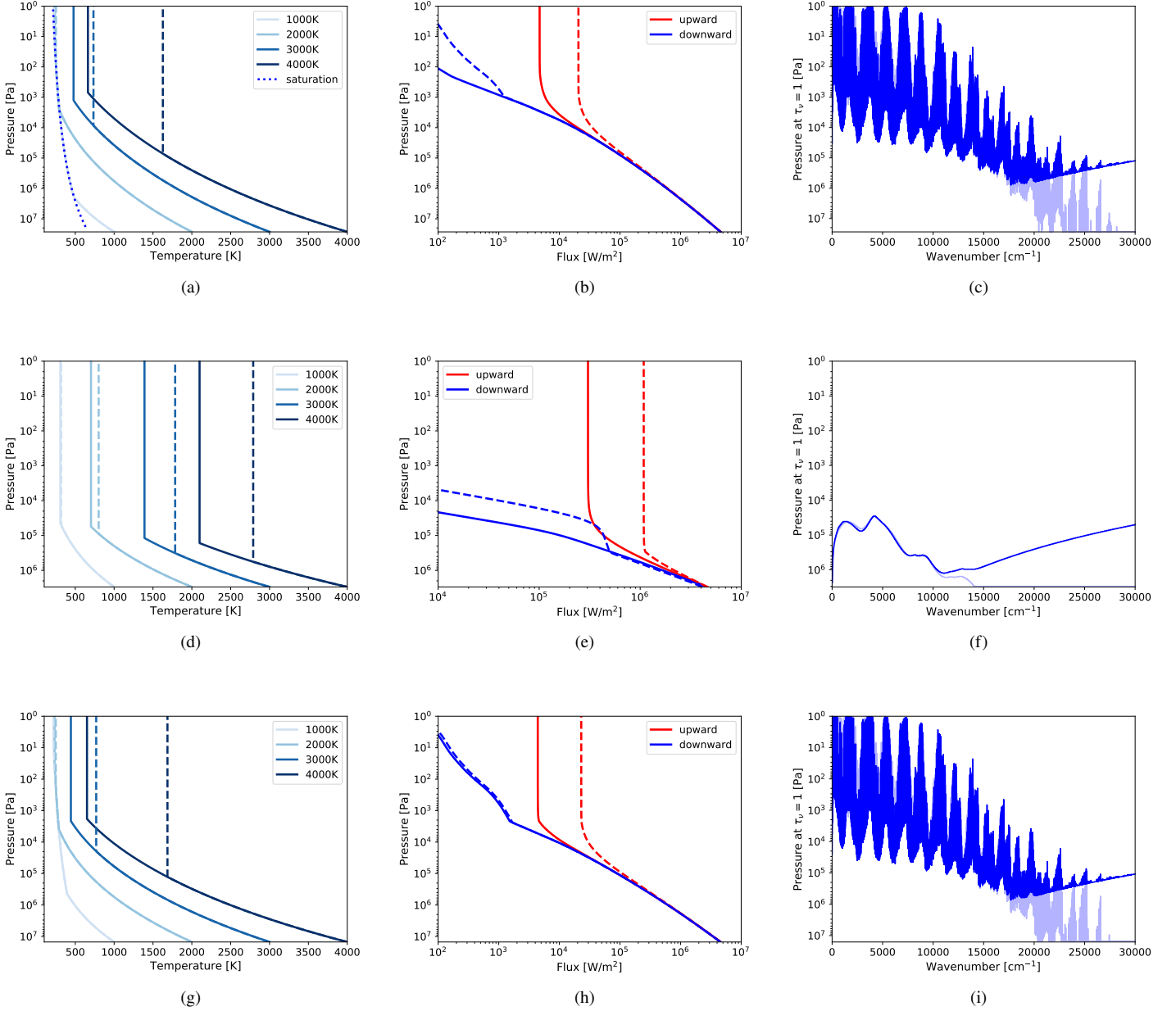
Figure 2. (a) Temperature profile in the pure H_2O atmosphere with the total hydrogen amount of N_{TO}. Here N_{TO} is the molecular number of hydrogen in the present-day terrestrial seawater. The solid and dashed lines represent the profiles with and without the Rayleigh scattering blanketing effects, respectively. Line colors represent variations in the surface temperature. The blue dotted line is the H_2O saturation vapor pressure. (b) Profile of the upward and downward planetary radiation flux in the pure H_2O atmosphere with the total hydrogen amount of N_{TO} and the surface temperature of 3000 K. The red and blue lines represent the upward and downward fluxes, respectively. The solid and dashed lines represent the profiles with and without the Rayleigh scattering blanketing effects, respectively. (c) Pressure where $\tau_\nu = 1$ with wavenumber in the pure H_2O atmosphere with the total hydrogen amount of N_{TO} and the surface temperature of 3000 K. The dark and light blue lines represent the values with and without the Rayleigh scattering blanketing effects, respectively. (d), (e), and (f) are the same as (a), (b), and (c), respectively, but for the pure H_2 atmosphere with the total hydrogen amount of N_{TO}. (g), (h), and (i) are the same as (a), (b), and (c), respectively, but for the H_2O-H_2 atmosphere with the molar H_2/H_2O ratio of unity and the total hydrogen amount of N_{TO}.
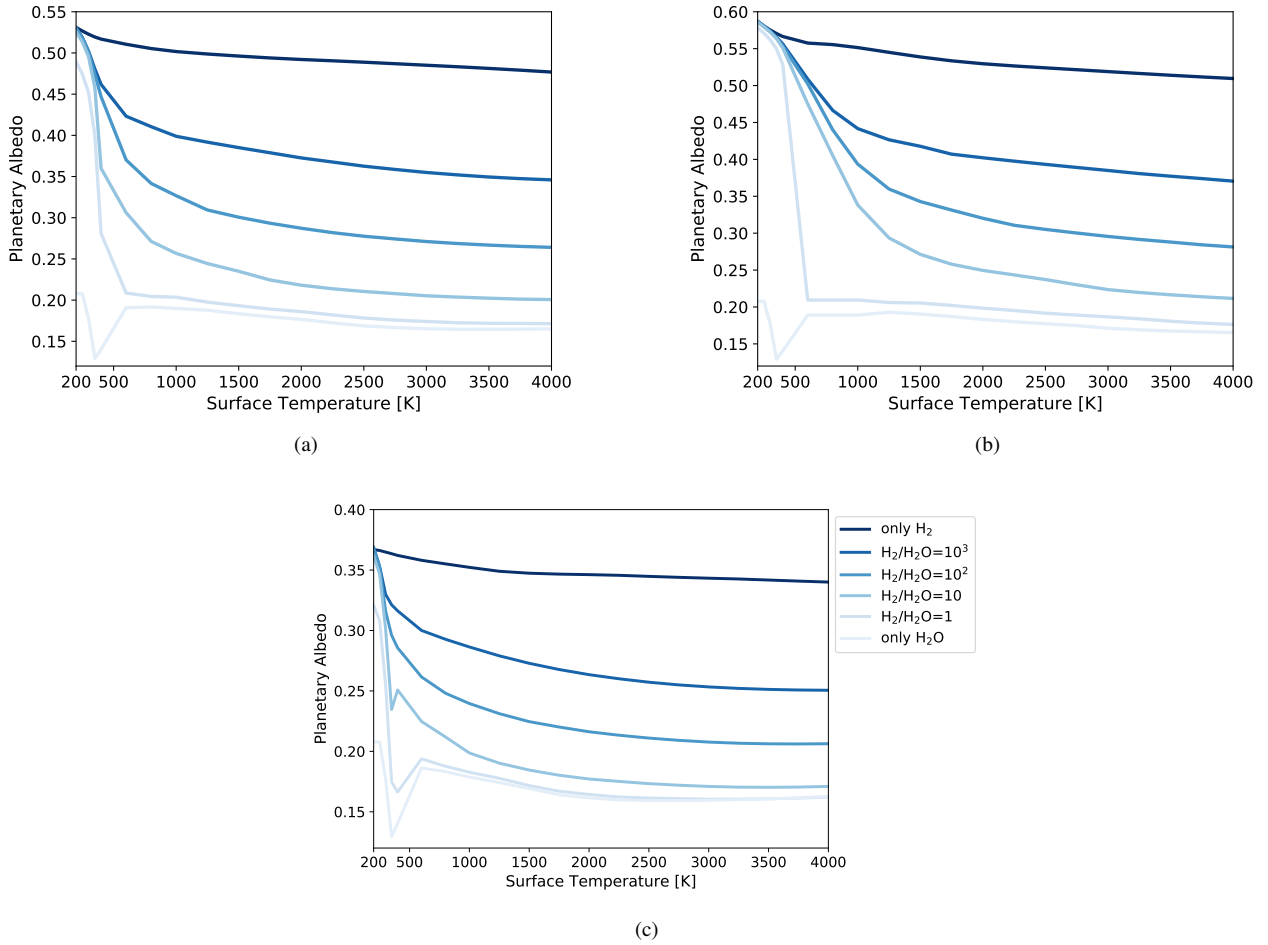
Figure 3. Planetary albedo with surface temperature when the total hydrogen molecular numbers in the atmosphere with seawater are $1N_{\mathrm{TO}}$ (a), $10N_{\mathrm{TO}}$ (b), and $0.1N_{\mathrm{TO}}$ (c), respectively. Here N_{TO} is the hydrogen molecular number in the present-day terrestrial seawater. Line colors show variations in the molar H_2/H_2O ratio in the atmosphere with seawater.

(Figure 2(c)). The effect of Rayleigh scattering is also displayed in the vertical profile of the planetary radiation flux (Figure 2(b)), where the flux is significantly suppressed in the scattering case compared to the no-scattering case near and above the pressure level where Rayleigh scattering optical depth becomes unity. This suppression of OLR by the scattering results in a temperature drop in the upper atmosphere (Figure 2(a)), leading to a reduction in OLR at low wavenumbers below $\sim 20000\,\mathrm{cm}^{-1}$ (Figure 1(b)). In certain surface temperature ranges, OLR remains nearly constant regardless of surface temperature (Figure 1(a)). This is known as the radiation limit, which occurs when the atmospheric profile and radiative flux become fixed due to H_2O saturation around the levels where the optical depth is about unity (Nakajima et al. 1992). The H_2O saturation is shown in the coincidence of H_2O pressure and its saturation vapor pressure under radiation-limit conditions in Figure 2(a).

Rayleigh scattering is also effective in atmospheres including H_2 (Figures 1(c)–(f); Figures 2(d)–(i)). In pure H_2 atmospheres, OLR is suppressed through the H_2-H_2 collision-induced absorption at wavenumbers below $\sim 15000\,\mathrm{cm}^{-1}$, as well as through Rayleigh scattering (Figures 1(c) and (d); Figures 2(e) and (f)). Compared to pure H_2O atmosphere cases, the pressure level for the optical depth to reach unity tends to be high (Figures 2(e) and (f)). In the case when the H_2/H_2O ratio is unity, both the H_2O absorption and H_2-H_2 collision-induced absorption work effectively along with Rayleigh scattering (Figure 1(f); Figures 2(h) and (i)), leading to the lower OLR than that of the pure H_2 cases (Figure 1(e)).

The planetary albedo depending on the surface temperature, atmospheric mass, and composition is shown in Figure 3. The planetary albedo is strongly influenced by the atmospheric H_2/H_2O ratio, increasing with higher ratios due to a decrease in stellar absorption by H_2O under H_2-rich conditions. Higher total atmospheric mass also enhances the albedo through more
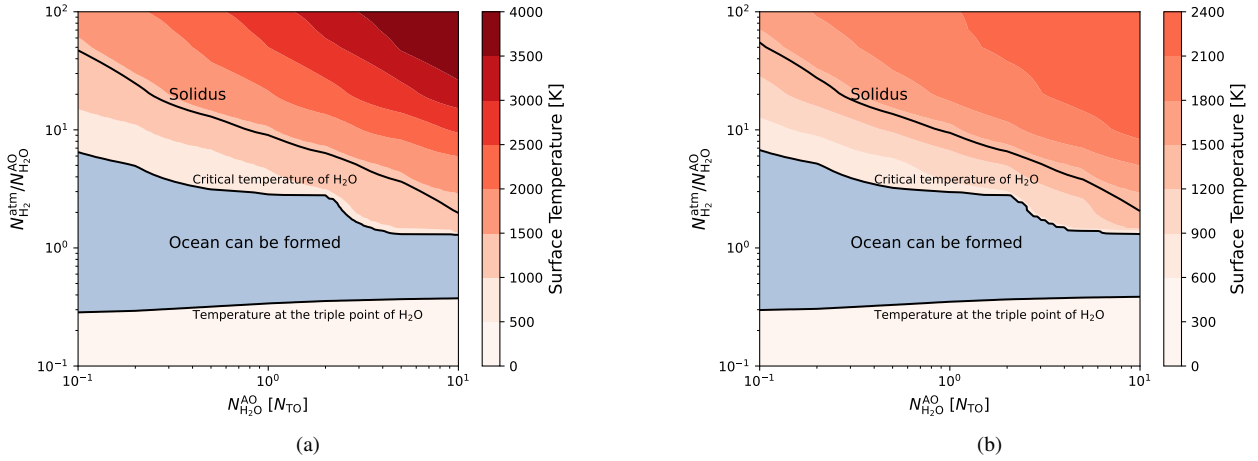
Figure 4. Equilibrium surface temperature where OLR equals net absorbed solar flux as a function of amounts of H_2O and H_2 on the planetary surface. (a) and (b) are the results with and without the scattering blanketing effects, respectively. The horizontal axis $N_{H_2O}^{AO}$ is the hydrogen molecular number of H_2O in the atmosphere with seawater normalized by the hydrogen molecular number in the present-day terrestrial seawater (N_{TO}). The vertical axis $N_{H_2}^{atm}/N_{H_2O}^{AO}$ is the ratio of the atmospheric hydrogen molecular number of H_2 to the hydrogen molecular number of H_2O in the atmosphere with seawater. The black lines represent the solidus temperature, the critical temperature of H_2O, and the temperature at the triple point of H_2O from the top. In the blue regions, surface temperatures are between the temperature at the triple point and the critical temperature, where oceans can be formed.

effective scattering at high pressures, as shown in the comparisons among Figure 3(a), (b), and (c). The gradual decreases in planetary albedo with increasing surface temperature are driven by an increased atmospheric H_2O abundance, broadening of H_2O absorption lines (e.g., Rothman et al. 2010), and the enhanced absorption coefficient of the H_2-H_2 collision-induced absorption at higher temperatures (e.g., Borysow 2002). Although this study assumes solar-type stellar flux, planetary albedo also depends on the stellar type. In particular, albedo is expected to significantly decrease for cooler stars, as stellar emission shifts to longer wavelengths, leading to stronger atmospheric absorption and weaker Rayleigh scattering of stellar irradiation (Kopparapu et al. 2013; Pluriel et al. 2019).

To clarify the fundamental relationship between planetary and solar radiation, equilibrium surface temperature, where OLR as shown in Figure 1 equals net absorbed solar flux derived from planetary albedo (Figure 3) and Equation (19) under fixed atmospheric mass and composition, is shown in Figures 4. The equilibrium surface temperature increases as the amounts of H_2O and H_2 increase due mainly to the suppression of OLR. The scattering blanketing effect further enhances this OLR suppression, leading to higher surface temperatures, particularly when H_2O and H_2 are abundant, as shown in the comparison between Figures 4(a) and 4(b). Consequently, the equilibrium surface temperature exceeds the solidus temperature at high atmospheric masses and H_2/H_2O ratios. For $H_2/H_2O \sim 1$, the equilibrium surface temperature lies between the triple point and the critical temperature of H_2O, suggesting that oceans can be formed under such conditions. Although a parameter space where oceans can exist appears under the solar flux at Earth's orbit, this would vanish under much higher stellar fluxes exceeding the radiation limit, as in the case of Venus's orbit. As the H_2/H_2O ratio decreases, the equilibrium surface temperature becomes less sensitive to total atmospheric mass and more influenced by the H_2/H_2O ratio. This occurs partly because the increase in planetary albedo associated with the increase in atmospheric amount, which leads to a decrease in surface temperature, offsets the decrease in OLR that contributes to temperature increase. In H_2-depleted conditions, the equilibrium surface temperature little depends on the total H_2O amount because the atmospheric profile is determined by the saturation vapor pressure.

3.2. *Thermal evolution of magma ocean and atmosphere*

In this section, we estimate the thermal co-evolution of the magma ocean and atmosphere by applying the calculated planetary and solar radiation fluxes as functions of surface temperature, atmospheric amount, and composition. The total amounts of H_2O and H_2 are treated as free parameters. As described in Section 2.3 in detail, the cooling and solidification of the magma ocean is supposed to be along with the net energy balance of the incoming and outgoing radiation at the top of the atmosphere. We also consider the partitioning of volatiles between the atmosphere and interior as described in Section 2.4. For simplicity, we neglect atmospheric escape to space, chemical interaction between the magma ocean and atmosphere, and the accretion of materials that
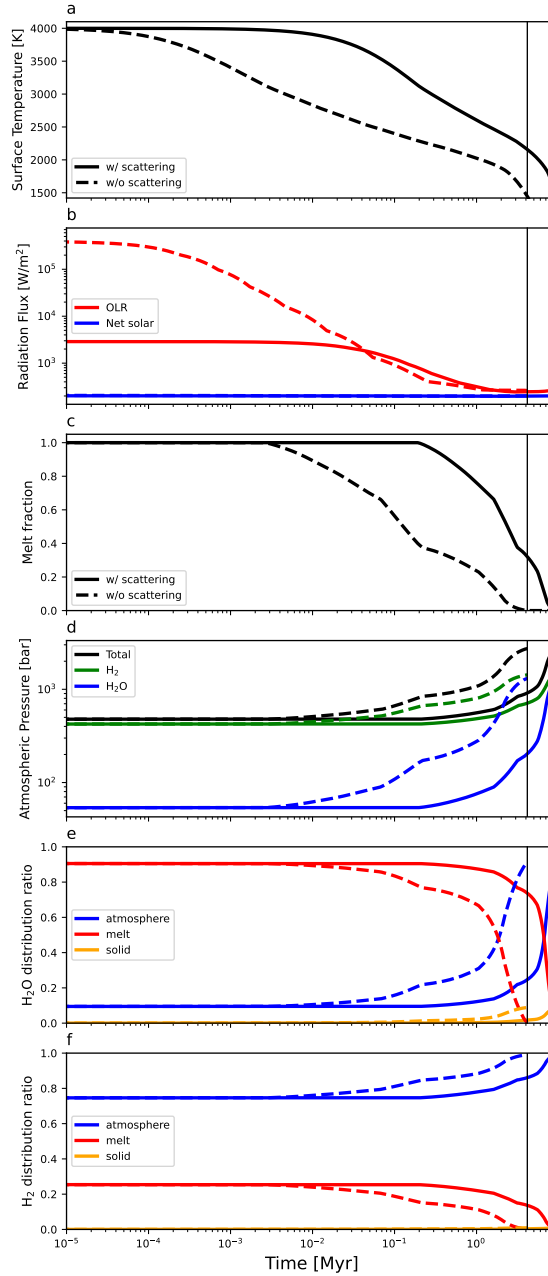
Figure 5. An example of the thermal evolution of magma ocean and atmosphere when the total amounts of both H_2O and H_2 are $10N_{TO}$. Here N_{TO} is the hydrogen molecular number in the present-day terrestrial seawater. The solid and dashed lines represent the results with and without the scattering blanketing effect, respectively. The vertical black lines represent the time when the magma ocean solidification finished in the case without scattering. (a) Surface temperature with time. (b) Radiation flux with time. The red lines represent OLR and the blue lines represent the net absorbed solar flux. (c) Melt fraction in the whole mantle. (d) Atmospheric pressure with time. The black line, green line, and blue line represent the total surface pressure, partial surface pressure of H_2, and partial surface pressure of H_2O, respectively. (e) The distribution ratio of H_2O among the atmosphere, melt, and solid. The blue, red, and orange lines represent the ratios of the atmosphere, melt, and solid, respectively. (f) The distribution ratio of H_2 among the atmosphere, melt, and solid. The blue, red, and orange lines represent the ratios of the atmosphere, melt, and solid, respectively.
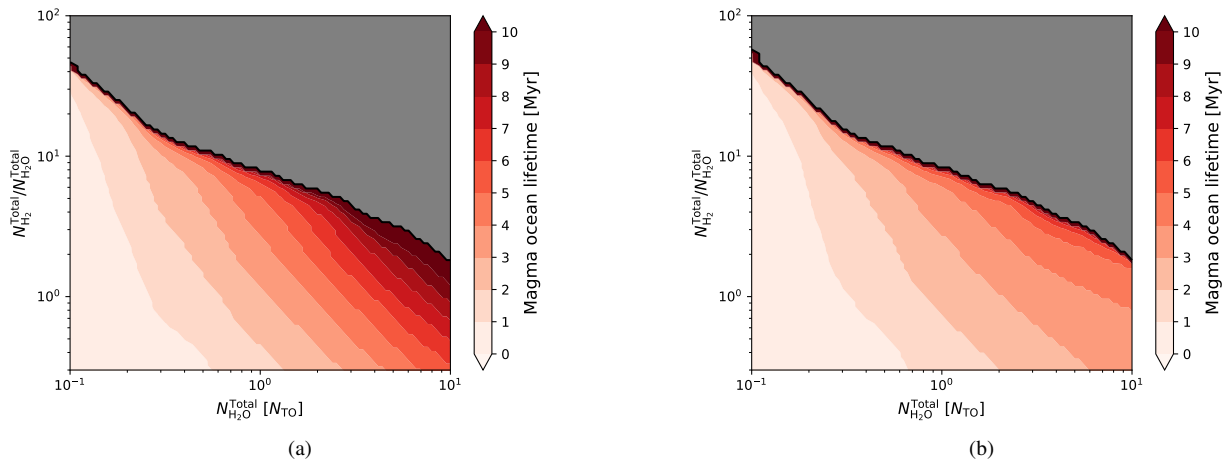
Figure 6. Lifetime of the magma ocean, defined as the duration over which the surface temperature remains above the solidus temperature, as a function of the total amounts of H_2O and H_2. (a) and (b) are the results with and without the scattering blanketing effects, respectively. The horizontal axis is the total hydrogen molecular number of H_2O normalized by the molecular number of hydrogen in the present-day terrestrial seawater (N_{TO}). The vertical axis is the ratio of the total amount of H_2 to that of H_2O. In the grey region, the equilibrium surface temperature exceeds the solidus temperature.

could supply volatiles or induce chemical reactions. We stop the evolution calculations either when the surface temperature drops below the solidus temperature or when the integration time exceeds 50 Myr. We define the magma ocean lifetime as the duration over which the surface temperature remains above the solidus temperature.

Figure 5 presents an example of the thermal evolution of a magma ocean and atmosphere when the total amounts of both H_2O and H_2 are $10N_{TO}$. In the early stages, the surface temperature is high and the atmosphere is H_2-dominated due to more efficient partitioning of H_2O into the melt as described in Equation (25) and its Henrian coefficient (Figures 5(a), 5(d)–(f)). During this stage, the scattering blanketing effect significantly suppresses OLR (Figure 5(b)). Consequently, the magma ocean maintains relatively high-temperature and high-melt fraction with the scattering blanketing effect (Figures 5(a) and 5(c)). As the magma ocean cools and solidifies via planetary radiation, H_2O degassing from the magma ocean progresses (Figures 5(d) and 5(f)), further contributing to OLR suppression (Figure 5(b)). The magma ocean lifetime is 9.7 Myr with the scattering blanketing effect, compared to 4.2 Myr without it.

Magma ocean lifetime as a function of total amounts of H_2O and H_2 are shown in Figure 6. The lifetime naturally extends as the total amounts of H_2O and H_2 increase, primarily due to the suppression of OLR. As shown in the comparison between Figures 6(a) and 6(b), the scattering blanketing effect on the magma ocean lifetime becomes increasingly pronounced with larger total amounts of H_2O and H_2, extending the lifetime by up to about three times. In the grey region of Figure 6, equilibrium between OLR and absorbed solar flux is achieved at certain stages, sustaining the equilibrium surface temperature above the solidus temperature. This indicates that the magma ocean state can persist as long as the atmospheric mass and composition remain unchanged by processes such as atmospheric escape or chemical interaction with the magma ocean in the ranges of total H_2O and H_2 amounts.

4. DISCUSSION

4.1. *Effects of uncertainties in assumptions*

4.1.1. *Upper atmospheric temperature*

Although the upper atmospheric temperature is set equal to the skin temperature in our model, it can deviate from the skin temperature in non-grey atmospheres (e.g., Wordsworth & Pierrehumbert 2013; Leconte et al. 2013). Figure 7 illustrates the effects of variations in upper atmospheric temperature on OLR. Overall, OLR is largely insensitive to the assumed upper atmospheric temperature because the upper atmosphere is optically thin. However, when the upper atmospheric temperature becomes significantly higher than the skin temperature, OLR increases, as this deviation affects the temperature profile near the level where the optical depth reaches unity. Previous non-grey radiative transfer calculations for H_2O-rich atmospheres have shown that the upper atmospheric temperature tends to be lower than the skin temperature because the upper atmosphere can absorb
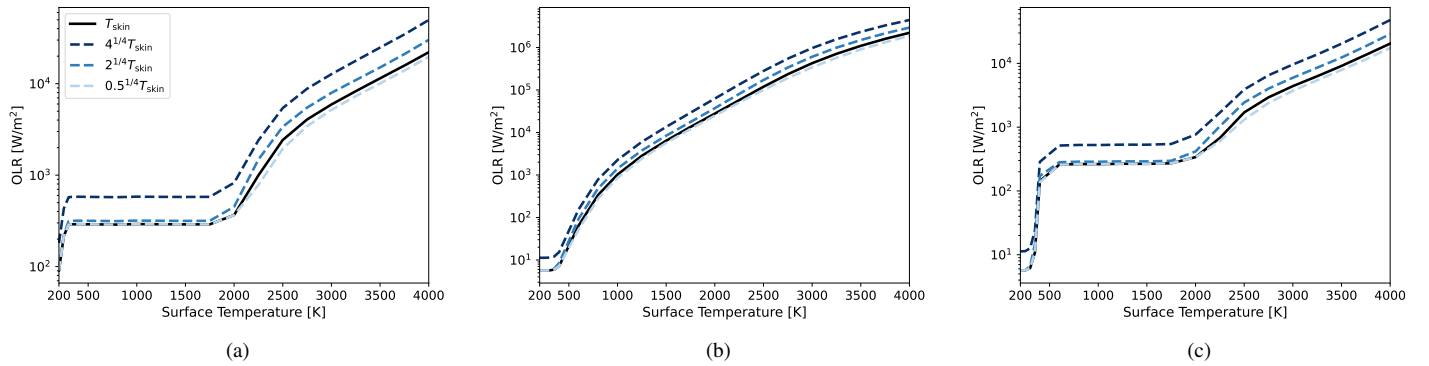
Figure 7. Outgoing longwave radiation (OLR) as a function of surface temperature with different upper atmospheric temperatures, for a pure H_2O atmosphere (a), a pure H_2 atmosphere (b), and an H_2O-H_2 atmosphere with a molar H_2/H_2O ratio of unity (c). The black lines represent results with the upper atmospheric temperature set to the skin temperature T_{skin}, while the dashed lines represent results for other upper atmospheric temperatures deviating from the skin temperature. In all cases, the atmospheric total hydrogen amount is N_{TO}, corresponding to the molecular number of hydrogen in the present-day terrestrial seawater.

upwelling infrared radiation only in limited spectral regions while remaining an efficient emitter (Wordsworth & Pierrehumbert 2013; Leconte et al. 2013). In light of this behavior, variations in the upper atmospheric temperature are expected to have little impact on OLR and the magma ocean lifetime in our calculations.

4.1.2. *Fully convective atmospheric structure*

Although we assumed that the atmosphere is fully convective below the stratosphere following the majority of previous studies, Selsis et al. (2023) and Nicholls et al. (2025) show that thick proto-atmospheres can become stable against convection and develop a nearly isothermal radiative layer in high-pressure regions due to the absorption of most stellar irradiation in the upper atmosphere, under energy equilibrium condition between planetary and stellar radiation. Figure 8 presents the effects of such radiative layer formation at pressures greater than 100 bar on OLR. OLR becomes higher by a factor in cases with a deep isothermal layer when the temperature near the level where the optical depth reaches unity increases. Detail investigations of convective stability under extremely high internal heat flux, as considered in this study, are important aspects to be explored in future studies.

Furthermore, H_2O condensation in H_2-rich atmospheres can also suppress convection by forming a gradient in the atmospheric mean molecular weight, leading to the formation of a super-adiabatic radiative layer in deep regions (Leconte et al. 2017, 2024). This convective inhibition can lower the temperature at and above the super-adiabatic radiative layer for a given surface temperature, thereby reducing OLR and prolonging the magma ocean lifetime. Investigating this condensation-induced convective inhibition is also part of our key future work for understanding the evolution of magma oceans and surface conditions under H_2-rich atmospheres.

4.1.3. *Cloud-free atmosphere*

Although our 1-D model neglects the radiative effects of clouds for simplicity, clouds can significantly influence the atmospheric thermal structure and radiative energy balance (Leconte et al. 2013; Charnay et al. 2013; Pluriel et al. 2019). In particular, they can substantially enhance the planetary albedo. To assess the potential impact, Figure 9 compares the magma ocean lifetime under an H_2O atmosphere with a fixed high planetary albedo of 0.9, the upper limit estimated by Pluriel et al. (2019), to that in the nominal case with a planetary albedo of ∼ 0.2, derived from our model and shown in Figure 3. In the high-albedo case, the magma ocean lifetime is reduced by up to about a factor of three due to the less efficient absorption of incoming stellar radiation. The actual lifetime is expected to fall between the values obtained in the nominal and high-albedo cases. A more detailed investigation of cloud effects is therefore crucial for accurately determining the magma ocean lifetime.

4.2. *Chemical evolution of a proto-atmosphere and magma ocean*

Although this study simplifies the chemical evolution in a proto-atmosphere and magma ocean to focus on the blanketing effect and thermal evolution, it is important to note that the redox states of both the magma ocean and the proto-atmosphere may have changed dramatically over time. During core-mantle differentiation, the magma ocean was likely highly reducing, with a redox state below the iron-wüstite buffer (e.g., Frost et al. 2008). Assuming chemical equilibrium with the magma ocean, the
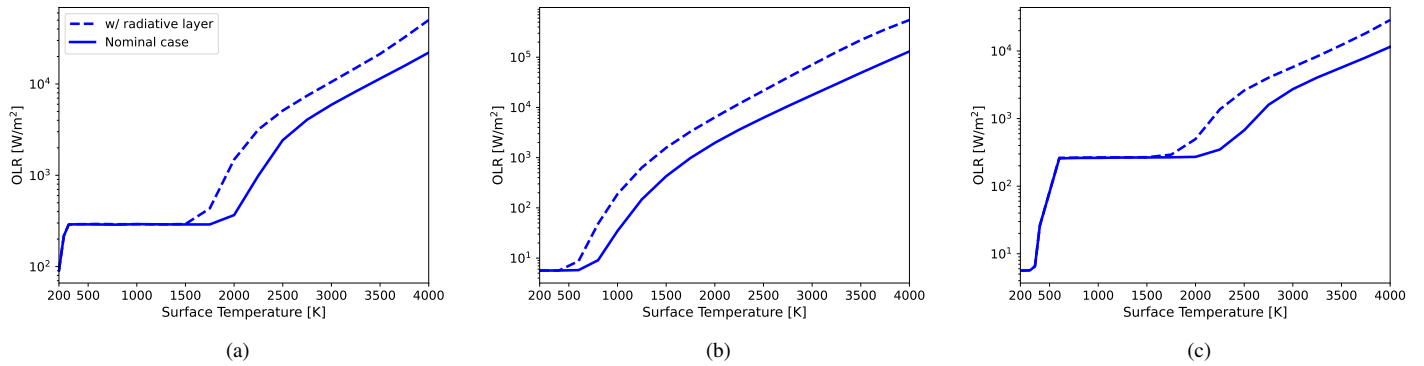
Figure 8. Outgonig longwave radiation (OLR) as a function of surface temperature for cases with an isothermal radiative layer at pressures greater than 100 bar (dashed), compared to cases without the radiative layer (solid; standard case), shown for a pure H_2O atmosphere (a), a pure H_2 atmosphere (b), and an H_2O-H_2 atmosphere with a molar H_2/H_2O ratio of unity (c). In all cases, the surface pressure is set to 270 bar, corresponding to the total atmospheric mass equivalent to that of the present-day terrestrial seawater.
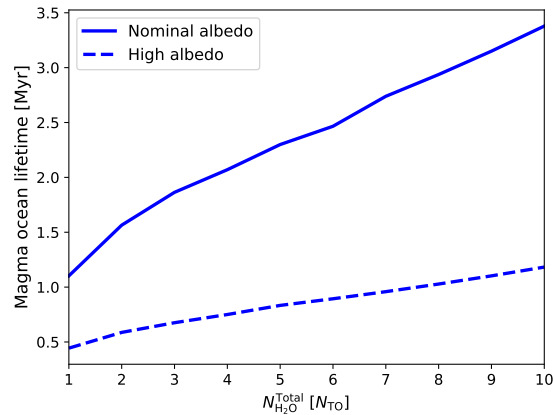

Figure 9. Lifetime of the magma ocean, defined as the duration over which the surface temperature remains above the solidus temperature, under an H_2O atmosphere with a nominal planetary albedo of ~ 0.2, derived from our model and shown in Figure 3 (solid line), and a fixed high planetary albedo of 0.9 (dashed line). The horizontal axis is the total hydrogen molecular number of H_2O normalized by the molecular number of hydrogen in the present-day terrestrial seawater (N_{TO}).

proto-atmosphere would have mainly consisted of reduced species such as H_2, CH_4, and CO (e.g., Kuramoto & Matsui 1996; Hirschmann 2012). Following the completion of core-mantle differentiation, the redox disproportionation of ferrous iron (Fe^{2+}) to ferric iron (Fe^{3+}) and metallic iron may have oxidized the magma ocean to the redox level observed in Earth's mantle today, through the sequestration of metallic iron into the core and the homogenization of iron oxides via vigorous convection (e.g., Armstrong et al. 2019; Deng et al. 2020; Kuwahara et al. 2023; Zhang et al. 2024). Interaction with this oxidized magma ocean would have further oxidized the proto-atmosphere, such as conversion of H_2 into H_2O.

Hydrodynamic escape, driven by intense X-ray and extreme ultraviolet (XUV) irradiation from the young Sun, likely also altered the composition of the proto-atmosphere. In H_2-rich atmospheres containing carbon-bearing species and H_2O, H_2 is estimated to escape at rates $\lesssim 1$ bar/Myr while other heavier species largely remain, due to radiative cooling of the outflow by radiatively active species, under early solar XUV conditions (Yoshida & Kuramoto 2021; Yoshida et al. 2022; Yoshida et al. 2024b). Although the rate is estimated to be slow, the preferential loss of H_2 can enhance the magma ocean cooling.

Photochemical processes likely also impacted proto-atmospheric composition. Reduced species such as CH_4 and CO should be converted into more oxidized species and various organics in the upper atmosphere, where molecular photolysis occurs (e.g., Zahnle et al. 2020; Wogan et al. 2023; Yoshida et al. 2024a). However, these photochemical products may have decomposed in the hot, lower atmosphere while the magma ocean remained. The accumulation of photochemical products likely began after the

surface temperature dropped enough to allow surface ocean formation. At this stage, CH_4 photolysis would primarily produce heavier organics due to their UV self-shielding effects, which suppress the production of oxidant radicals such as OH followed by the H_2O photolysis, and the accumulation of organics on the surface, potentially linked to the emergence of living organisms, may have proceeded (Yoshida et al. 2024a).

4.3. *Effects of the prolonged magma ocean lifetime on chemical differentiation*

The prolonged lifetime of the magma ocean due to the blanketing effect is expected to influence its chemical differentiation. Abe (1997) theoretically demonstrated that differentiation between compatible and incompatible elements tends to be limited in the lower mantle compared to the upper mantle due to the rapid cooling not enough for melt-solid separation to take place in the case without a proto-atmosphere. On the other hand, the effective blanketing effect of a proto-atmosphere can prolong the magma ocean lifetime even in the high-pressure regions of the lower mantle. Figure 10 shows the time required for the temperature at a pressure of 23 GPa, which is the boundary between the lower and upper mantle, to reach the solidus temperature. The solidification time increases with the abundances of H_2O and H_2, reaching or exceeding ~ 1 Myr which is comparable with the time required for melt-solid separation to take place in the upper mantle estimated by Abe (1997), across a wide range of initial conditions. These results indicate the differentiation between compatible and incompatible elements can efficiently occur in the lower mantle region as well as the upper mantle under a thick proto-atmosphere. In the lower mantle region, bridgmanite is expected to be the first phase to crystallize from the magma ocean (e.g., Boukaré et al. 2015; Caracas et al. 2019). Efficient crystal settling could result in a chemical composition distinct from the upper mantle, such as a different Mg/Si ratio, as indicated by some geochemical studies of igneous rocks derived from plumes (e.g., Murakami et al. 2024). Additionally, differentiation in the lower mantle may be related to chemical heterogeneities reflected in variations in seismic velocities (e.g., Garnero & McNamara 2008).

4.4. *Implications of the prolonged magma ocean lifetime for Moon formation*

The extension of the magma ocean phase due to the blanketing effect could have crucial implications for the Moon's formation. Precise geochemical measurements of lunar samples reveal a remarkable similarity in isotopic compositions between the Moon and Earth (e.g., Melosh 2014). However, numerical models of the Moon-forming giant impact suggest that most of the Moon's material originated from the impactor (e.g., Canup 2004b), making it challenging to naturally explain this isotopic resemblance to Earth. To address this discrepancy, Karato (2014) and Hosono et al. (2019) proposed that a giant solid impactor hit the proto-Earth while it was covered with a magma ocean. In such a scenario, a substantial portion of the ejected Moon-forming material would derive from this magma ocean, aligning with the observed isotopic similarity between the Moon and Earth. Additionally, this model can account for the Moon's higher FeO content compared to bulk silicate Earth, as FeO preferentially partitions into melt over coexisting minerals (e.g., Mibe et al. 2006).

To assess the influence of the proto-atmosphere's blanketing effect, we estimate the probability of giant impacts occurring during the magma ocean phase. Geochronological data on lunar samples such as Hf–W isotopic systematics indicates that the Moon formed by a giant impact about 50–150 Myr after the formation of CAIs (e.g., Jacobsen 2005; Jacobson et al. 2014; Fischer & Nimmo 2018; Thiemens et al. 2019; Canup et al. 2023). Supposing that Earth experienced about ten times giant impacts, the average time interval of giant impacts is expected to have been 5–15 Myr. Figure 11 shows the probability $P_{\rm imp}$ that one or more giant impacts occurred during the magma ocean phase, calculated using a Poisson distribution:

$$P_{\rm imp} = 1 - \exp\left(-\frac{\tau_{\rm MO}}{\tau_{\rm imp}}\right), \tag{26}$$

where $\tau_{\rm MO}$ is the magma ocean lifetime in Figure 6 and $\tau_{\rm imp}$ is the average interval between giant impacts. Here $\tau_{\rm imp}$ is set to be 10 Myr, and $\tau_{\rm MO}$ is assumed to be 50 Myr under equilibrium conditions between OLR and net solar absorption (grey regions in Figure 6). The prolonged magma ocean lifetime due to the scattering blanketing effect increases the probability of a giant impact occurring during the magma ocean phase. For instance, the probability increases from 0.34 to 0.62 by the scattering blanketing effect when the total amounts of both H_2O and H_2 are $10N_{\rm TO}$. This enhanced probability provides a compelling explanation for the Moon's observed chemical and isotopic characteristics, supporting the hypothesis of a magma ocean origin of the Moon.

5. CONCLUSIONS

We developed a 1-D radiative transfer model for planetary and solar radiation in proto-atmospheres composed of H_2O and H_2 and a coupled thermal evolution model of interiors and proto-atmospheres to investigate the scattering blanketing effect on planetary radiation and magma ocean cooling. Our results show that Rayleigh scattering significantly reduces outgoing planetary
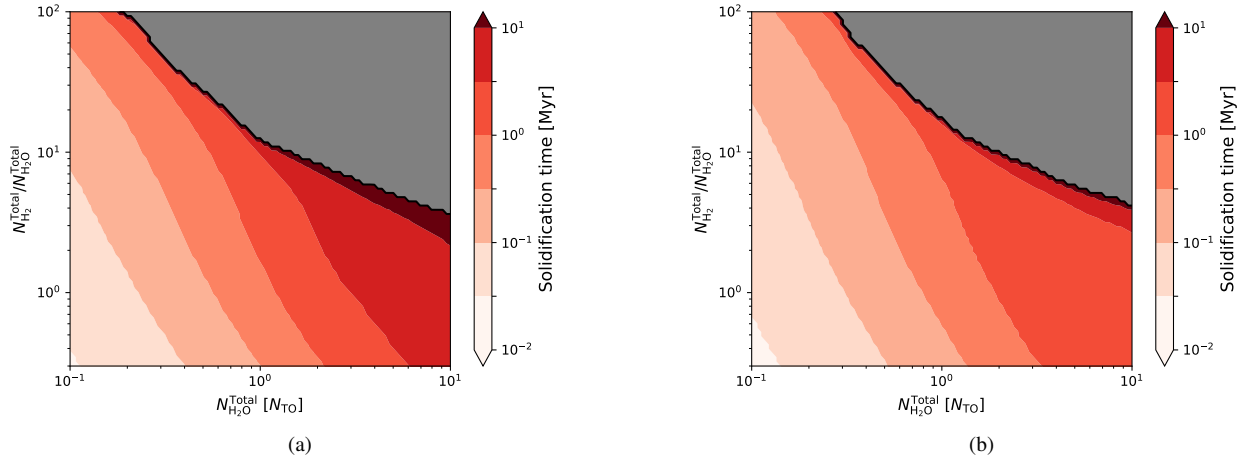
Figure 10. Time required for the temperature at a pressure of 23 GPa to reach the solidus temperature as a function of the total amounts of H_2O and H_2. (a) and (b) are the results with and without the scattering blanketing effects, respectively. The horizontal axis is the total amount of H_2O normalized by the molecular number of hydrogen in the present-day terrestrial seawater (N_{TO}). The vertical axis is the ratio of the total amount of H_2 to that of H_2O. In the grey region, the equilibrium temperature at this region exceeds the solidus temperature.
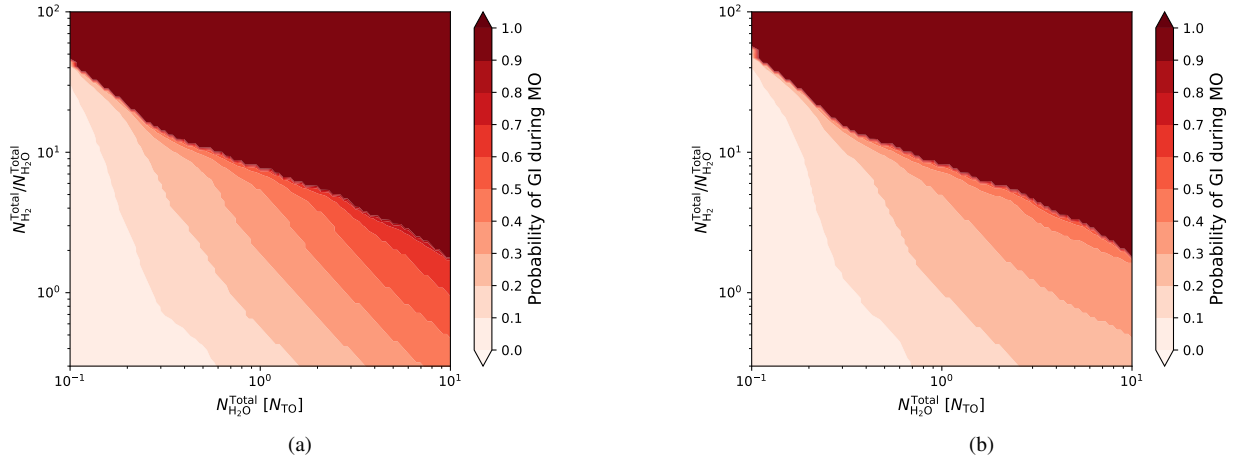

Figure 11. Probability of at least one giant impact occurring during the magma ocean phase, as described by Equation (26). The average time interval between giant impacts is set at 10 Myr. (a) and (b) are the results with and without the scattering blanketing effects, respectively. The horizontal axis is the total amount of H_2O normalized by the molecular number of hydrogen in the present-day terrestrial seawater (N_{TO}). The vertical axis is the ratio of the total amount of H_2 to that of H_2O.

radiation at wavelengths below $\sim 1\,\mu$m, particularly in hot, thick atmospheres where scattering is highly effective. Consequently, the planetary outgoing radiation flux decreases by up to about one to two orders of magnitude, and the magma ocean lifetime is prolonged by up to about three times due to the scattering blanketing effect when the total amounts of H_2O and H_2 are equivalent to or greater than the present-day terrestrial seawater. These findings suggest that the prolonged magma ocean phase facilitated efficient differentiation between compatible and incompatible elements, even in the lower mantle. Furthermore, they imply that a sustained magma ocean likely persisted throughout much of the giant impact phase, supporting a magma ocean origin of the Moon consistent with its observed chemical characteristics.

REFERENCES

Abe, Y. 1997, Physics of the Earth and Planetary Interiors, 100, 27

Abe, Y., & Matsui, T. 1985, Journal of Geophysical Research: Solid Earth, 90, C545

—. 1986, Journal of Geophysical Research: Solid Earth, 91, E291

—. 1988, Journal of the Atmospheric Sciences, 45, 3081

Armstrong, K., Frost, D. J., McCammon, C. A., Rubie, D. C., & Boffa Ballaran, T. 2019, Science, 365, 903

Barth, P., Carone, L., Barnes, R., et al. 2021, Astrobiology, 21, 1325

Borysow, A. 2002, Astronomy & Astrophysics, 390, 779

Borysow, A., Jørgensen, U. G., & Fu, Y. 2001, Journal of Quantitative Spectroscopy and Radiative Transfer, 68, 235

Boukaré, C.-E., Ricard, Y., & Fiquet, G. 2015, Journal of Geophysical Research: Solid Earth, 120, 6085

Bower, D. J., Hakim, K., Sossi, P. A., & Sanan, P. 2022, The planetary science journal, 3, 93

Bower, D. J., Kitzmann, D., Wolf, A. S., et al. 2019, Astronomy & Astrophysics, 631, A103

Canup, R. M. 2004a, Icarus, 168, 433

—. 2004b, Annu. Rev. Astron. Astrophys., 42, 441

Canup, R. M., Righter, K., Dauphas, N., et al. 2023, Reviews in Mineralogy and Geochemistry, 89, 53

Caracas, R., Hirose, K., Nomura, R., & Ballmer, M. D. 2019, Earth and Planetary Science Letters, 516, 202

Charnay, B., Forget, F., Wordsworth, R., et al. 2013, Journal of Geophysical Research: Atmospheres, 118, 10

Chase, M. W. 1998, J. of Physical and Chemical Reffernce Data, 1529

Deng, J., Du, Z., Karki, B. B., Ghosh, D. B., & Lee, K. K. 2020, Nature communications, 11, 2007

Eisenberg, D., & Kauzmann, W. 1969, The structure and properties of water (Oxford University Press, USA)

Elkins-Tanton, L. T. 2008, Earth and Planetary Science Letters, 271, 181

—. 2012, Annual Review of Earth and Planetary Sciences, 40, 113

Fiquet, G., Auzende, A., Siebert, J., et al. 2010, Science, 329, 1516

Fischer, R. A., & Nimmo, F. 2018, Earth and planetary science letters, 499, 257

Frost, D., Mann, U., Asahara, Y., & Rubie, D. 2008, Philosophical Transactions of the Royal Society A: Mathematical, Physical and Engineering Sciences, 366, 4315

Garnero, E. J., & McNamara, A. K. 2008, science, 320, 626

Goldblatt, C., Robinson, T. D., Zahnle, K. J., & Crisp, D. 2013, Nature Geoscience, 6, 661

Gough, D. 1981, in Physics of Solar Variations: Proceedings of the 14th ESLAB Symposium held in Scheveningen, The Netherlands, 16–19 September, 1980, Springer, 21–34

Hamano, K., Abe, Y., & Genda, H. 2013, Nature, 497, 607

Hamano, K., Kawahara, H., Abe, Y., Onishi, M., & Hashimoto, G. L. 2015, The Astrophysical Journal, 806, 216

Herzberg, C., Raterron, P., & Zhang, J. 2000, Geochemistry, Geophysics, Geosystems, 1

Hirschmann, M. M. 2000, Geochemistry, Geophysics, Geosystems, 1

—. 2012, Earth and Planetary Science Letters, 341, 48

Hosono, N., Karato, S.-i., Makino, J., & Saitoh, T. R. 2019, Nature Geoscience, 12, 418

Hu, R., Seager, S., & Bains, W. 2012, The Astrophysical Journal, 761, 166

Ikoma, M., Elkins-Tanton, L., Hamano, K., & Suckale, J. 2018, Space Science Reviews, 214, 1

Jacobsen, S. B. 2005, Annu. Rev. Earth Planet. Sci., 33, 531

Jacobson, S. A., Morbidelli, A., Raymond, S. N., et al. 2014, Nature, 508, 84

Johnson, R. D. 1998, NIST computational chemistry comparison and benchmark database, American Institute of Chemical Engineers

Karato, S.-i. 2014, Proceedings of the Japan Academy, Series B, 90, 97

Kasting, J. F. 1988, Icarus, 74, 472

Katyal, N., Nikolaou, A., Godolt, M., et al. 2019, The Astrophysical Journal, 875, 31

Katyal, N., Ortenzi, G., Grenfell, J. L., et al. 2020, Astronomy & Astrophysics, 643, A81

Kopparapu, R. K., Ramirez, R., Kasting, J. F., et al. 2013, The Astrophysical Journal, 765, 131

Kuramoto, K., & Matsui, T. 1996, Journal of Geophysical Research: Planets, 101, 14909

Kuwahara, H., Nakada, R., Kadoya, S., Yoshino, T., & Irifune, T. 2023, Nature Geoscience, 16, 461

Lebrun, T., Massol, H., Chassefière, E., et al. 2013, Journal of Geophysical Research: Planets, 118, 1155

Leconte, J., Forget, F., Charnay, B., Wordsworth, R., & Pottier, A. 2013, Nature, 504, 268

Leconte, J., Selsis, F., Hersant, F., & Guillot, T. 2017, Astronomy & Astrophysics, 598, A98

Leconte, J., Spiga, A., Clément, N., et al. 2024, Astronomy & Astrophysics, 686, A131

Lichtenberg, T., Bower, D. J., Hammond, M., et al. 2021, Journal of Geophysical Research: Planets, 126, e2020JE006711

Marcq, E. 2012, Journal of Geophysical Research: Planets, 117

Marcq, E., Salvador, A., Massol, H., & Davaille, A. 2017, Journal of Geophysical Research: Planets, 122, 1539

Massol, H., Davaille, A., & Sarda, P. 2023, Journal of Geophysical Research: Planets, 128, e2023JE007848

Massol, H., Hamano, K., Tian, F., et al. 2016, Space Science Reviews, 205, 153

Matsui, T., & Abe, Y. 1986a, Nature, 319, 303

—. 1986b, Nature, 322, 526

Maurice, M., Dasgupta, R., & Hassanzadeh, P. 2024, Astronomy & Astrophysics, 688, A47, doi: 10.1051/0004-6361/202347749

Melosh, H. 2014, Philosophical Transactions of the Royal Society A: Mathematical, Physical and Engineering Sciences, 372, 20130168

Mibe, K., Orihashi, Y., Nakai, S., & Fujii, T. 2006, Geophysical Research Letters, 33

Mlawer, E., Cady-Pereira, K., Mascio, J., & Gordon, I. 2023, Journal of Quantitative Spectroscopy and Radiative Transfer, 306, 108645

Murakami, M., Khan, A., Sossi, P. A., Ballmer, M. D., & Saha, P. 2024, Annual Review of Earth and Planetary Sciences, 52, 605

Nakajima, S., Hayashi, Y.-Y., & Abe, Y. 1992, Journal of the Atmospheric Sciences, 49, 2256

Nicholls, H., Lichtenberg, T., Bower, D. J., & Pierrehumbert, R. 2024, Journal of Geophysical Research: Planets, 129, e2024JE008576

Nicholls, H., Pierrehumbert, R. T., Lichtenberg, T., Soucasse, L., & Smeets, S. 2025, Monthly Notices of the Royal Astronomical Society, 536, 2957

Nikolaou, A., Katyal, N., Tosi, N., et al. 2019, The Astrophysical Journal, 875, 11

Peng, D.-Y., & Robinson, D. B. 1976, Industrial & Engineering Chemistry Fundamentals, 15, 59

Pierrehumbert, R. T. 2010, Principles of planetary climate (Cambridge University Press)

Pluriel, W., Marcq, E., & Turbet, M. 2019, Icarus, 317, 583

Rothman, L. S., Gordon, I., Barber, R., et al. 2010, Journal of Quantitative Spectroscopy and Radiative Transfer, 111, 2139

Rothman, L. S., Gordon, I. E., Babikov, Y., et al. 2013, JQSRT, 130, 4, doi: 10.1016/j.jqsrt.2013.07.002

Salvador, A., Massol, H., Davaille, A., et al. 2017, Journal of Geophysical Research: Planets, 122, 1458

Schaefer, L., Wordsworth, R. D., Berta-Thompson, Z., & Sasselov, D. 2016, The Astrophysical Journal, 829, 63

Selsis, F., Leconte, J., Turbet, M., Chaverot, G., & Bolmont, É. 2023, Nature, 620, 287

Solomatov, V. 2007, Evolution of the Earth, 9, 91

Thiemens, M. M., Sprung, P., Fonseca, R. O., Leitzke, F. P., & Münker, C. 2019, Nature Geoscience, 12, 696

Toon, O. B., McKay, C., Ackerman, T., & Santhanam, K. 1989, Journal of Geophysical Research: Atmospheres, 94, 16287

Wogan, N. F., Catling, D. C., Zahnle, K. J., & Lupu, R. 2023, The Planetary Science Journal, 4, 169

Wordsworth, R., Kalugina, Y., Lokshtanov, S., et al. 2017, Geophysical Research Letters, 44, 665

Wordsworth, R., & Pierrehumbert, R. 2013, The Astrophysical Journal, 778, 154

Yoshida, T., Koyama, S., Nakamura, Y., Terada, N., & Kuramoto, K. 2024a, Astrobiology, 24, 1074

Yoshida, T., & Kuramoto, K. 2021, Monthly Notices of the Royal Astronomical Society, 505, 2941

Yoshida, T., Terada, N., Ikoma, M., & Kuramoto, K. 2022, ApJ, 934, 137, doi: 10.3847/1538-4357/ac7be7

Yoshida, T., Terada, N., & Kuramoto, K. 2024b, Progress in Earth and Planetary Science, 11, 59

Yurchenko, S. N., Al-Refaie, A. F., & Tennyson, J. 2018, Astronomy & Astrophysics, 614, A131

Zahnle, K., Arndt, N., Cockell, C., et al. 2007, Space Science Reviews, 129, 35

Zahnle, K. J., Kasting, J. F., & Pollack, J. B. 1988, Icarus, 74, 62

Zahnle, K. J., Lupu, R., Catling, D. C., & Wogan, N. 2020, The Planetary Science Journal, 1, 11

Zhang, H. L., Hirschmann, M. M., Lord, O. T., et al. 2024, Science Advances, 10, eadp1752

Zhang, J., & Herzberg, C. 1994, Journal of Geophysical Research: Solid Earth, 99, 17729